2013 IEEE 10th International Symposium on Biomedical Imaging:
From Nano to Macro
San Francisco, CA, USA, April 7-11, 2013

CO-OCCURRING GLAND TENSORS IN LOCALIZED CLUSTER GRAPHS: QUANTITATIVE HISTOMORPHOMETRY FOR PREDICTING BIOCHEMICAL RECURRENCE FOR INTERMEDIATE GRADE PROSTATE CANCER

George Lee[⋆1], *Rachel Sparks*[1], *Sahirzeeshan Ali*[2], *Anant Madabhushi*[⋆2]

[1] Rutgers, The State University of New Jersey
Dept. of Biomedical Engineering, NJ
[2] Case Western Reserve University
Dept. of Biomedical Engineering, OH

Michael D. Feldman[3], *Stephen R. Master*[3], *Natalie Shih*[3], *John E. Tomaszewski*[4]

[3] University of Pennsylvania
Dept. of Pathology and Anatomical Sciences, PA
[4] University at Buffalo - SUNY
Dept. of Pathology and Laboratory Medicine, NY

ABSTRACT

Quantitative histomorphometry (QH), computational tools to analyze digitized tissue histology, has become increasingly important for aiding pathologists in assessing cancer severity. In this study, we introduce a novel set of QH features utilizing co-occurring gland tensors (CGT) in localized cluster graphs to quantitatively evaluate prostate cancer (CaP) histology. CGTs offer three main advantages over previous QH features: 1) gland tensors represent a novel measurement that has been anecdotally described as one of interest, but never quantitatively modeled, 2) CGTs extract measurements based on local rather than global glandular networks, constructed using cluster graphs, and 3) second order statistical features (energy, homogeneity, energy, and correlation) obtained from a co-occurrence matrix capture the spatial interactions of gland tensors in the image. We extract 4 CGT features from 56 regions across 40 intermediate grade CaP patients and evaluated the ability of CGT features to predict biochemical recurrence (BCR) within 5 years of radical prostatectomy. Intermediate Gleason score 7 cancers represent the predictive borderline for BCR cases, where 50% of cases develop BCR. We found that CGT features outperformed 5 different sets of QH features, previously shown to be effective in CaP grading, when evaluated via a Random Forest classifier (66% accuracy for CGT features versus 55% for the next closest QH feature set), all comparisons being statistically significant.

1. INTRODUCTION

Gleason scoring is a qualitative system which uses tissue morphology to assess prostate cancer (CaP) aggressiveness. However, Gleason scoring, in spite of the fact that it is the best available marker for CaP prognosis, is plagued by issues of inter- and intra-observer variability [1]. The recent advent of digital whole slide scanners has allowed for the development of quantitative histomorphometry (QH) algorithms for automated scoring and grading of digitized images of prostate histology.

Recently several researchers have attempted to develop automated, computerized Gleason grading algorithms for prostate pathology [2–6]. Graph tesselations of cell nuclei using Voronoi or Delaunay graphs have been found to be predictive of Gleason grade [2, 3]. The problem with such graph constructs are that they employ nuclei as vertices which means that (1) individual nuclei need to be accurately detected, (2) graph construction based off these individual nuclei involve edges that traverse the stromal and epithelial regions, diluting the contributions of the resulting features, and (3) traditional graph tesselations do not account for glandular morphology or architecture. While Naik et al. [5] and Sparks et al. [6] explicitly looked at gland morphology, there is anecdotal evidence to suggest that gland orientation may be prognostic of aggressive CaP. However, to the best of the authors' knowledge, gland directionality has not been explicitly modeled. CaP is fundamentally a disease of glandular disorganization and the extent of directionality loss has been suggested to be related to CaP grade. Normal benign glands align themselves with respect to the fibromusclar stroma, and thus display a coherent directionality. However, malignant prostate glands lose their capability to orient themselves and display no preferred directionality.

In this paper, we investigate a new set of features, co-occurring gland tensors (CGT), which aim to capture the directional information in localized gland networks within a co-occurrence matrix. Gray level texture features are commonly calculated from gray level co-occurrence matrices, and have been used successfully on numerous image classification applications [7], including digital pathology [2, 3]. For gray level texture features, local intensity patterns are found across the image and aggregated into a co-occurrence matrix.

CGTs leverage this idea to aggregate local gland tensor signatures across an image. The underlying assumption driving this work is that gland directionality can be quantified and that it can be used to differentiate aggressive CaP from intermediate Gleason scores.

2. CO-OCCURRING GLAND TENSORS

2.1. Automated Gland Detection and Segmentation

An automatic region-growing gland segmentation algorithm [8] is used to detect and segment boundaries on the histological image as shown in Figure 1(b). A probabilistic pair-wise markov random field model (PPMM) subsequently prunes out boundaries not pertaining to glands [8].

2.2. Capturing Gland Tensors

To determine the directionality for each gland γ_p, $p \in \{1, \ldots, n\}$, we perform principal component analysis on the set of boundary points $[x_p, y_p]$, constituting the gland, to obtain the principal components $A = [a_1, a_2]$. The first principal component a_1 describes the directionality of the gland in the form of the major axis, along which the greatest variance occurs in the gland boundary. The principal axis a_1 is converted to an angle $\theta(\gamma_p) \in [0°180°]$ counterclockwise from the vector $< 1, 0 >$, as shown in Figure 1(f).

2.3. Cluster Graph Construction

Local gland networks are difficult to quantify due to the variability in the size of the gland and stromal areas. Cluster graphs provide an adaptable neighborhood definition based on the density of glands. These neighborhoods subsequently provide windows for analysis of gland tensor signatures.

As such, we define the graph $G = \{V, E\}$, where V represents the set of n gland centroids $\gamma_i, \gamma_j \in V$, $i, j \in \{1, 2, \ldots, n\}$ as nodes, and E represents the set of edges which connect them. The edges between all pairs of nodes γ_i, γ_j are set as a probabilistic decaying function

$$E = \{(i, j) : r < d(i, j)^{-\alpha}, \forall \gamma_i, \gamma_j \in V\}, \qquad (1)$$

where $d(i, j)$ represents the Euclidean distance between γ_i and γ_j. $\alpha \geq 0$ controls the density of the graph (Figure 1(c)), where α approaching 0 generates highly connected graphs while α approaching ∞ generates sparser graphs. $r \in [0, 1]$ is an empirically defined threshold for edge construction.

2.4. Co-occurring Gland Tensors (CGT)

Gland tensor orientation does not lend itself towards probability distribution functions due to its inherently cyclical distribution. However, the co-occurrence matrix allows for interpretation of these gland tensors by collecting the frequency of co-occurrence of two tensors in a neighborhood.

In computing angle orientations, $\theta(\gamma_p)$ is discretized such that $\bar{\theta}(\gamma_p) = \omega * \text{floor}(\frac{\theta}{\omega})$. For each gland, $\gamma_i \in V$, we define a neighborhood $\mathcal{N}_p$, to include all $\gamma_j \in V$ where a path between γ_i and γ_j exists in graph G. We define a $b \times b$ co-occurrence matrix $\mathcal{C}$, such that for each neighborhood $\mathcal{N}_p$,

$$\underset{\gamma_i, \gamma_j \in \mathcal{N}_p}{\mathcal{C}_{\mathcal{N}_p}(\bar{\theta}_1, \bar{\theta}_2)} = \sum_{\substack{\theta_1, \theta_2 = 1 \\ \theta_1 \neq \theta_2}}^{b} \begin{cases} 1, & \text{if } \theta(\gamma_i) = \theta_1 \text{ and } \theta(\gamma_j) = \theta_2 \\ 0, & \text{otherwise} \end{cases} \qquad (2)$$

where $b = \frac{180}{\omega}$. $\mathcal{C}_{\mathcal{N}_p}(\bar{\theta}_1, \bar{\theta}_2)$ are aggregated such that

$$\mathcal{C}(\bar{\theta}_1, \bar{\theta}_2) = \frac{1}{n} \sum_{p=1}^{n} \mathcal{C}_{\mathcal{N}_p}(\bar{\theta}_1, \bar{\theta}_2). \qquad (3)$$

We then extract 4 CGT features from the directional co-occurrence matrix as described in Table 1.

Table 1. Description of CGT features

CGT Feature	Description
Entropy	$\sum_{\theta_1, \theta_2} -\mathcal{C}(\theta_1, \theta_2) \log(\mathcal{C}(\theta_1, \theta_2)))$
Homogeneity	$\sum_{\theta_1, \theta_2} \frac{\mathcal{C}(\theta_1, \theta_2)}{1 + \lvert\theta_1 - \theta_2\rvert}$
Energy	$\sum_{\theta_1, \theta_2} \mathcal{C}(\theta_1, \theta_2)^2$
Correlation	$\sum_{\theta_1, \theta_2} \frac{(\theta_1 - \mu\theta_1)(\theta_2 - \mu\theta_2)\mathcal{C}(\theta_1, \theta_2)}{\sigma_{\theta_1} \sigma_{\theta_2}}$

3. EXPERIMENTAL DESIGN AND RESULTS

3.1. Significance of Biochemical Recurrence in CaP

Each year, nearly 60,000 patients undergo radical prostatectomy (RP) treatment for CaP [9]. However, for 15-40% of RP patients, biochemical recurrence (BCR) occurs within 5 years [9]. BCR is commonly defined as a detectable persistence of prostate specific antigen (PSA) of at least 0.2 ng/ml, suggestive of recurring aggressive CaP [10]. Several studies have shown that the outcomes of intermediate Gleason score 7 cancers can vary considerably [11], and statistical tables suggest a 5-year BCR-free survival rate as low as 43% for such cases [12]. Therefore, we can assume a baseline classification rate of 50% for predicting BCR on Gleason score 7 cases based on visual analysis of CaP histology.

3.2. Data Acquisition and Description

The dataset (obtained from the Hospital at the University of Pennsylvania) is comprised of 40 CaP patients with intermediate Gleason scores (33 Gleason score 7, 5 Gleason 6, and 2 Gleason 8) and tumor stage T2 or T3, who had undergone RP. Of these patients, 20 were diagnosed with biochemical recurrence (BCR), and 20 had no recurrence (NR). The excised prostate was subsequently sliced, stained with hematoxylin and eosin (H&E), and digitized at a resolution of 0.5 μm per pixel. For each digitized image, CaP regions were annotated by a pathologist. In total, 56 regions were annotated, 28 from BCR patients and 28 from NR patients.

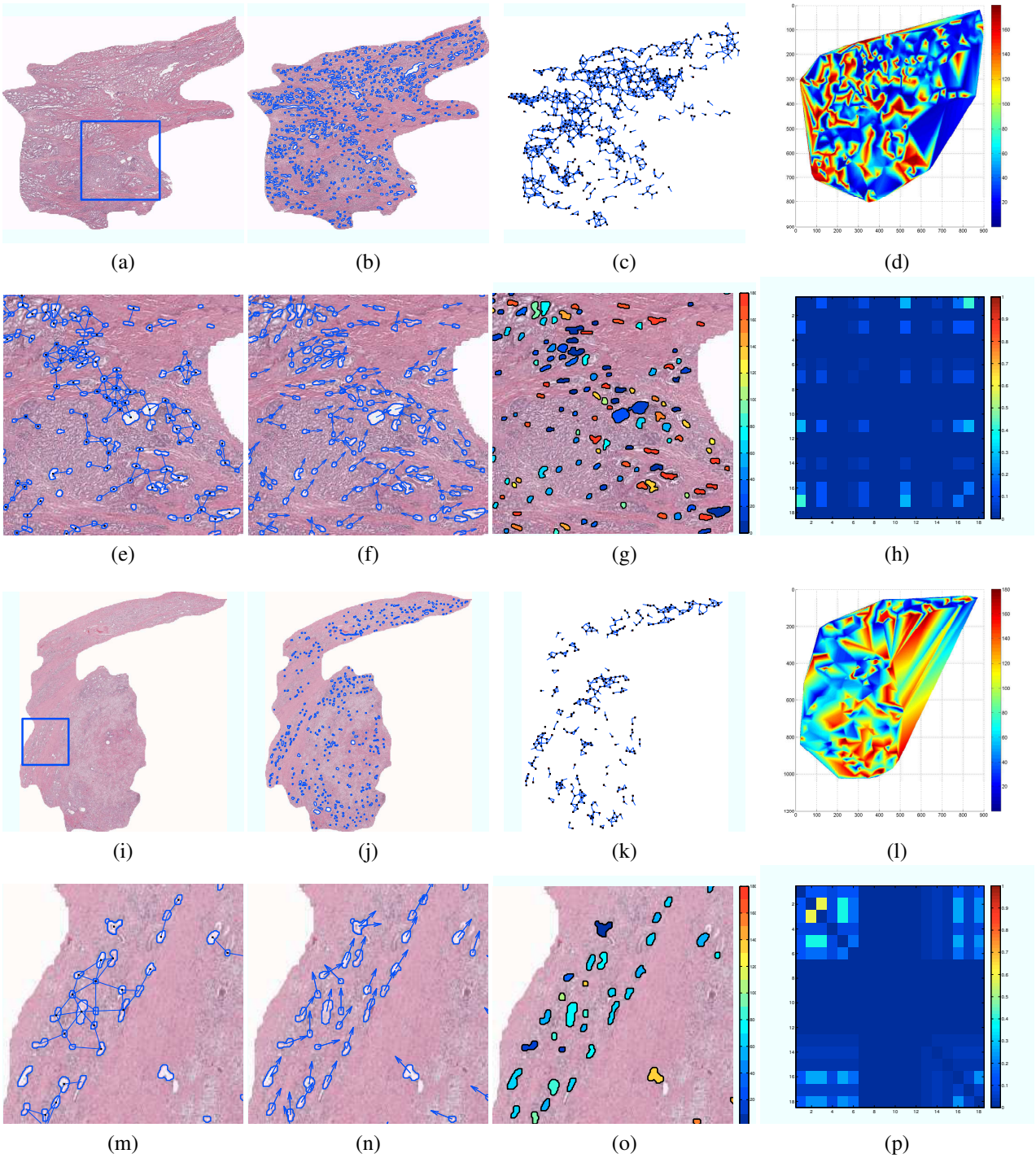

Fig. 1. (a) and (i) show annotated histological CaP regions pertaining to a (a)-(h) BCR and a (i)-(p) NR case study, respectively. (b),(j) Automated gland segmentation defines the gland boundaries and locations [8]. (c),(k) Cluster graphs are formed by connecting neighboring glands. (d),(l) A heatmap of the cancer region reveals areas of similar gland tensors, where colors (blue to red) pertains to an angle θ from 0° to 180° degrees. (e),(m) An enlarged view of the region of interest shown in (a) and (i), respectively, illustrates a localized gland network defined by the cluster graph. (f),(n) Arrows denote the directionality of each gland in the image. (g),(o) A colormap (blue to red) provides an alternate representation of gland tensors corresponding to angles $\theta \in [0^\circ, 180^\circ]$. (h),(p) A heatmap of the resulting co-occurrence matrices denotes the frequency with which two glands of different directionalities co-occur in each neighborhood (blue is low co-occurrence and red is high co-occurrence).

Table 2. Mean and standard deviation in accuracy for 6 QH feature classes over 100 runs of Random Forest classification

QH Feature Sets	**#**	**Description of Selected Features**	**Accuracy** (%)
Gland Morphology	25	Area Ratio, distance Ratio, Standard Deviation of Distance, etc.	52.98 ± 5.00
Voronoi Diagram	12	Polygon area, perimeter, chord length: mean, std. dev., min/max ratio, disorder	54.58 ± 5.29
Delaunay Triangulation	8	Triangle side length, area: mean, std. dev., min/max ratio, disorder	54.55 ± 5.76
Minimum Spanning Tree	4	Edge length: mean, std. dev., min/max ratio, disorder	52.60 ± 5.71
Gray-Level Texture	14	Angular second moment, Contrast, Correlation, Entropy, etc	54.18 ± 5.57
Co-occurring Gland Tensors	4	Entropy, Homogeneity, Energy, Correlation	$\mathbf{66.13 \pm 5.22}$

3.3. QH Comparison via Random Forest Classification

Figure 1 illustrates the differences between a BCR and NR case in terms of the CGTs. Figures 1(f),(g) characterize the disorder in BCR cases. Figure 1(g), the glands appear as a large spectrum of colors, denoting the different directionalities in Figure 1(f). Conversely, for the NR case, the color visualization (Figure 1(l)) is more consistent, suggesting less variance in the gland orientation.

Figures 1(d),(l) provide a more global view of this disorder. In the BCR case, Figure 1(d) reveals rapid changes in color across the image, whereas the NR case (Figure 1(l)) shows smoother color transitions across the image. Most importantly, this disorder is captured via the co-occurrence matrices. Figure 1(h) demonstrates a scattered co-occurrence matrix pattern away from the diagonal, suggesting large angular dissimilarity in gland direction, whereas Figure 1(p) reveals the similarly directed glands in the local gland networks shown via large blocks in the co-occurrence matrix.

Table 2 reveals that over 100 iterations of randomized 3-fold cross validation via Random Forest classification, CGT features (66% accuracy) outperform 5 comparison QH feature sets (Gland Morphology, Voronoi, Delaunay, Minimum Spanning Tree, and Gray Level Texture) for predicting BCR. In all cases, CGT features were found to have a statistically significant ($p < 0.01$) improvement in classification accuracy compared to comparison QH feature sets.

These results suggest that gland orientation, an anecdotal attribute that has not been explicitly defined, may be capable of separating BCR and NR in cases that were previously indistinguishable. Furthermore, unlike previous graph based approaches that have been applied to CaP grading [2,3], cluster graphs provide an adaptive, local constraint such that CGTs are extracted from within tumor epithelial regions and hence are not affected by edges traversing the stroma and epithelium.

4. CONCLUDING REMARKS

In this paper, we have formalized the previously anecdotal descriptor for gland orientation and demonstrated its prognostic value towards stratifying patients with intermediate Gleason grade. The CGT features were found to yield a statistically significant improvement in distinguishing CaP patients at risk for BCR within 5 years compared to a number of QH features which had previously shown to be important for automated Gleason grading. For future work, we aim to further evaluate the CGT features on a larger cohort of patients.

5. REFERENCES

[1] WC Allsbrook, Jr et al., "Interobserver reproducibility of gleason grading of prostatic carcinoma: general pathologist.," *Hum Pathol*, vol. 32, no. 1, pp. 81–88, Jan 2001.

[2] WA Christens-Barry and AW Partin, "Quantitative grading of tissue and nuclei in prostate cancer for prognosis prediction.," *Johns Hopkins Apl Technical Digest.*, vol. 18, pp. 226–233, 1997.

[3] S. Doyle et al., "Cascaded discrimination of normal, abnormal, and confounder classes in histopathology: Gleason grading of prostate cancer," *BMC bioinformatics*, vol. 13, no. 1, pp. 282, 2012.

[4] A. Golugula et al., "Supervised regularized canonical correlation analysis: integrating histologic and proteomic measurements for predicting biochemical recurrence following prostate surgery," *BMC bioinformatics*, vol. 12, no. 1, pp. 483, 2011.

[5] S. Naik et al., "Automated gland and nuclei segmentation for grading of prostate and breast cancer histopathology," in *International Symposium on Biomedical Imaging*. IEEE, 2008, pp. 284–287.

[6] R. Sparks and A. Madabhushi, "Gleason grading of prostate histology utilizing manifold regularization via statistical shape model of manifolds," in *Proc. of SPIE Vol*, 2012, vol. 8315, pp. 83151J–1.

[7] R.M. Haralick et al., "Textural features for image classification," *IEEE Trans. on Systems, Man and Cybernetics*, , no. 6, pp. 610–621, 1973.

[8] JP Monaco et al., "High-throughput detection of prostate cancer in histological sections using probabilistic pairwise markov models.," *Med Image Anal*, vol. 14, no. 4, pp. 617–629, Aug 2010.

[9] BJ Trock et al., "Prostate cancer-specific survival following salvage radiotherapy vs observation in men with biochemical recurrence after radical prostatectomy.," *JAMA*, vol. 299, no. 23, pp. 2760–2769, Jun 2008.

[10] AV D'Amico et al., "Preoperative psa velocity and the risk of death from prostate cancer after radical prostatectomy.," *N Engl J Med*, vol. 351, no. 2, pp. 125–135, Jul 2004.

[11] JR Stark et al., "Gleason score and lethal prostate cancer: does 3 + 4 = 4 + 3?," *J Clin Oncol*, vol. 27, no. 21, pp. 3459–3464, Jul 2009.

[12] M Han et al., "Biochemical (prostate specific antigen) recurrence probability following radical prostatectomy for clinically localized prostate cancer.," *J Urol*, vol. 169, no. 2, pp. 517–523, Feb 2003.